Thin Solid Films 774 (2023) 139837

Contents lists available at ScienceDirect

Thin Solid Films

journal homepage: www.elsevier.com/locate/tsf

Facile synthesis of $NiSe_2$:α-Fe_2O_3 thin film: Physical, optical and photoelectronic properties

Eran Visser [a], Neville Cory [a], Orlette Mkhari [a], Jessica Chamier [b], Franscious Cummings [c], Mahabubur Chowdhury [a,*]

[a] Nanomaterial Research Group (NRG), Department of Chemical Engineering, Cape Peninsula University of Technology, Bellville, 7535, South Africa
[b] Department of Chemical Engineering, Centre for Catalysis Research, HySA Catalysis, University of Cape Town, Cape Town 7700, South Africa
[c] Electron Microscope Unit, University of the Western Cape, Bellville-7535, South Africa

ARTICLE INFO

Keywords:
Photoelectronic
Electrodeposition
Thin film
Ferric oxide
Facile synthesis
α-Fe_2O_3

ABSTRACT

In this study, a highly scalable approach to fabricating $NiSe_2$:α-Fe_2O_3 heterojunction thin film in the absence of a dehydration step or lattice parameter matching was established. The attachment of $NiSe_2$ to α-Fe_2O_3 leads to an 82% and 97% decrease in charge transfer resistance (with and without illumination respectively) compared to pristine α-Fe_2O_3. The magnitude of the open circuit potential increased from approximately -0.30 V to -0.42 V vs Ag/AgCl, providing a stronger electric field for charge carrier separation. Charge transfer efficiency was calculated by using a ratio of charge carriers removed and those produced in the bulk. Scanning electron microscopy coupled with the electrodeposition current-time transients study proved that the attachment process involved the progressive nucleation of $NiSe_2$ and the simultaneous cathodic reduction of α-Fe_2O_3.

1. Introduction

Hematite (Fe_2O_3) has long been considered a promising material for solar powered water splitting due to its stability, abundance, suitable band gap (2.0 – 2.2 eV); and its band positioning makes it an ideal photoanode [1–3]. The material, however, is limited in application due to its poor conductivity, short carrier lifetime, short hole diffusion length, and poor charge mobility [4,5]. Many strategies have been employed to improve the performance of hematite-based photocatalysts including adding co-catalysts [6,5], metal dopants [7,6], as well as inorganic [8] and organic [9] semiconductors. As a result of the ongoing research into hematite-based materials, these materials have been able to reach photocurrents as high as 4.6 mA/cm^2 at 1.23 V vs reversible hydrogen electrode and a solar to hydrogen conversion efficiency of 4.8% when used in tandem with a perovskite solar cell [4]. However, this improvement is still not efficient enough to be commercially feasible.

A possible strategy is combining hematite with metal selenides (MS). MS can have excellent photocatalytic properties [10,11] and many are p-type with optimal band gaps for water splitting as depicted in Fig. 1 [12–14]. To date, there is a scarcity in the literature that focuses on selenide attachment to hematite. One such work considered the attachment of PbSe quantum dots to hematite nanowires [15]. The dehydration of the hematite enabled PbSe nucleation onto the hematite surface. The inherently small percent mismatch of epitaxial supercell parameters allowed the two crystal faces to join seamlessly.

Electrodeposition is a highly scalable technique that allows for the rapid synthesis of nanomaterials. However, A major challenge for the electrodeposition of MS is the application of a negative potential to the hematite. The Fe^{3+} in hematite is in its highest oxidation state and is vulnerable to reduction reactions as shown by the Pourbaix diagram in Fig. 2 [16]. Literature concerned with preventing the cathodic reduction of α-Fe_2O_3 is scarce because more common goals are to prevent oxidation [17], or even promote the reduction [18,19], with effort to combat corrosion. Various studies found that the electrical reduction of α-Fe_2O_3 can be promoted by high solution temperature [18,19], introduction of reducing gasses such as H_2 or CO [19] applied potentials of greater than 1.4 V (cathodic) [18], and use of a highly alkaline environment [18,20], Contradictory to the literature, this study showed that the integrity of the α-Fe_2O_3 layer under negative potential can be maintained by avoiding the aforementioned conditions.

The charge transfer resistance is usually associated with the inverse of the electrochemical reaction rate, such that a lower value is desirable [21,22]. It has been reported that the doping of hematite with precious

* Corresponding author.
E-mail address: chowdhurym@cput.ac.za (M. Chowdhury).

https://doi.org/10.1016/j.tsf.2023.139837
Received 6 February 2022; Received in revised form 4 April 2023; Accepted 6 April 2023
Available online 7 April 2023

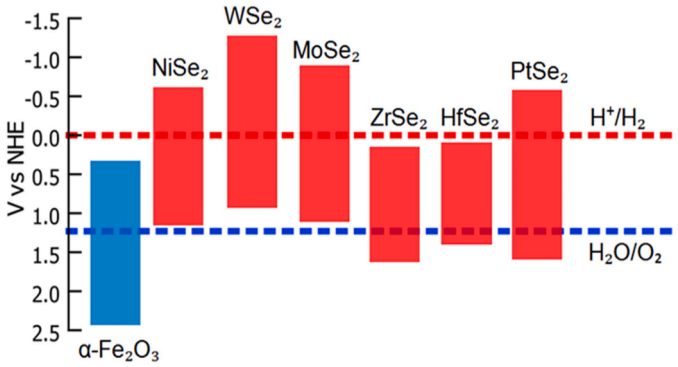

Fig. 1. Band positions for hematite and some complementary p-type metal selenides.

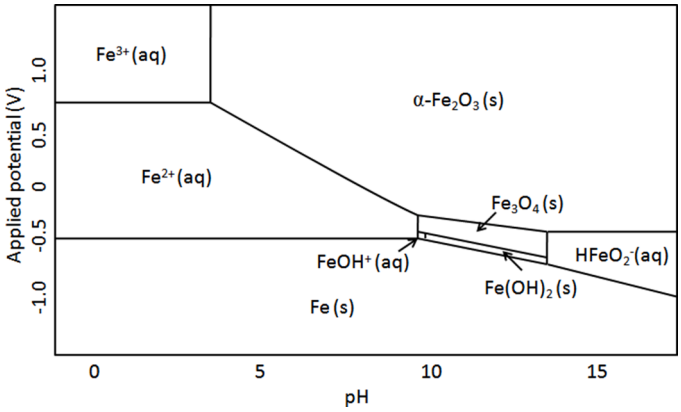

Fig. 2. Pourbaix diagram for the Iron-water system at [Fe] $= 10^{-5}$ M/kg.

metals such as germanium reduces the charge transfer resistance [4]. This work intends to achieve the same result with readily available materials coupled with a facile synthesis procedure to allow for rapid scalability. It has also been proven that an increase in the magnitude of the open circuit potential (OCP) is indicative of superior water splitting capabilities [23].

Herein, we report the synthesis of a α-Fe_2O_3:$NiSe_2$ thin film electrode using electrodeposition without the requirement of a dehydration step or crystal lattice parameter matching. Removing the dehydration step would ultimately result in a less energy intensive process and reduce capital costs as no vacuum is required. It must be noted that the study aims to explore the photoelectronic properties of the developed material rather than reporting on the photocatalytic properties. The developed method is highly scalable and opens the possibility of exploring many more combinations of metal oxides and MS materials.

2. Experimental procedure

2.1. Materials

All materials were used without further purification. HCl solution (37%), HNO_3 solution (70%), Acetone (95%), and Ethanol (95%) were obtained from Kimix, South Africa. Fluoride-doped tin oxide (FTO) glass (100 mm x 100 mm x 2.2 mm thick, resistivity ~ 7 Ω/sq), $FeCl_3$ anhydrous (97%), $NaNO_3$ (99%), $NiCl_2{\cdot}6H_2O$ (98%), Selenium powder (100-mesh, 99.5+%), LiCl (98%), HNO_3 solution (68%) were obtained from Merck, South Africa.

2.2. Materials and methods

2.2.1. SeO_2 preparation

The SeO_2 powder used in synthesis was prepared by combining 10 g of Selenium powder in 250 mL of 68% HNO_3. The solution was transferred to a round bottom flask and placed on a heating mantle to boil for 3 h under vigorous stirring. Under these conditions, large amounts of NO gas were produced and safely vented. The excess solution was allowed to evaporate leaving behind SeO_2 crystals which were collected and stored in the dark.

2.2.2. FTO glass and α-Fe_2O_3/FTO preparation

The FTO glass (15 slides) was cut into rectangular slides of 20 mm x 30 mm x 2 mm and placed upright in glass vials. All the samples were initially subject to hydrothermal treatment of an FTO glass slide in a glass vial with a plastic top. Each FTO glass slide was placed into a 20 ml glass vial and the vials were filled to the brim with a solution containing 10% dish soap and 90% de-ionised water by volume. A separate beaker containing the plastic tops was also filled with dish soap solution to cover the plastic tops. This beaker and the vials were sonicated for 30 min. After sonication the vials with slides and the beaker were emptied and rinsed with de-ionised water. The previous step was then repeated using a 50/50% v/v mixture of ethanol and acetone. The previous step was then repeated with de-ionised water. The de-ionised water was poured out. The vials with the slides and the beaker containing the plastic tops were dried in a convection oven at 40 °C for 3 h. Once completely dry the plastic tops were placed on the vials containing the glass slides.

Thereafter, a solution of 15 mM $FeCl_3$ and 67.5 mM $NaNO_3$ was prepared in 100 mL de-ionised water under constant stirring for 5 min. The solution was topped-up with de-ionised water to 150 mL and stirred again. Of this solution, 7 mL was transferred into each of the FTO-containing glass vials and capped. The vials were placed in a convection oven at 80 °C for 4 h, forming β-FeOOH nanorods. The slides were removed and rinsed with de-ionised water before being dried at 40 °C for 1 h in a convection oven. The slides were then calcined at 700 °C for 32 min in a muffle furnace to convert the β-FeOOH to α-Fe_2O_3.

2.2.3. $NiSe_2$:α-Fe_2O_3 synthesis

The electrodeposition solution was prepared by adding 19.5 mM $NiCl_2$, 0.3 mM SeO_2, and 60 mM LiCl to 300 mL de-ionised water at room temperature under constant stirring. The α-Fe_2O_3 slides were rinsed with acetone and placed upright in 20 mL of the electrodeposition solution. These slides were connected to a potentiostat as the working electrode, with an Ag/AgCl reference electrode and a carbon rod counter electrode. The electrodeposition was performed via linear sweep voltammetry in a potential window of 0 V to −0.464 V vs Ag/AgCl at a 10 mV/s scan rate and then maintaining an applied potential of −0.464 V for 90 s. These slides were then rinsed with de-ionised water, dried at 80 °C for an h, and annealed at 200 °C for 45 min in a furnace. A fresh electrodeposition solution was used for successive deposition samples. 0

2.2.4. Physical characterization

The crystal structures were identified using grazing incidence X-ray diffraction (XRD, PANalytical X'Pert PROPW3040/60). The XRD patterns were obtained in the 2-theta range of 20–80 °, the instrument was fitted with a Cu-Kα radiation source at wavelength of 0.154 at a tube voltage of 45 kV and 40 mA current with step size of 0.02 °/s. To analyze the sample surfaces X-ray photoelectron spectroscopy (XPS) measurements were made using a Thermo-ESCAlab 250Xi with monochromatic Al Kα source at 1486.6 eV, 300 W power in a 1×10^{-6} Pa, X-ray spot size of 900 μm, energy of 100 eV, and no sputtering was done. The binding energy scale is calibrated by manufacturer and is checked after routine maintenance by analysing a pure Cu sample. The binding energy scale of the group of spectra collected was not reference. For XPS peak area measurement and peak fitting, a Shirley background was used. The XPS

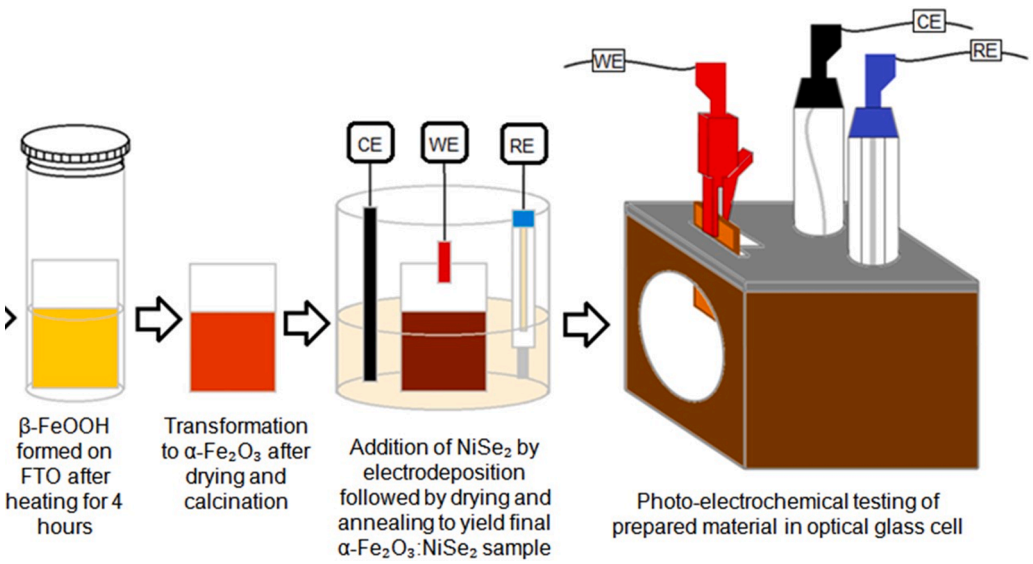

Fig. 3. A depiction of the synthesis and testing process. CE, WE, and RE depict the counter, working, and reference electrodes, respectively.

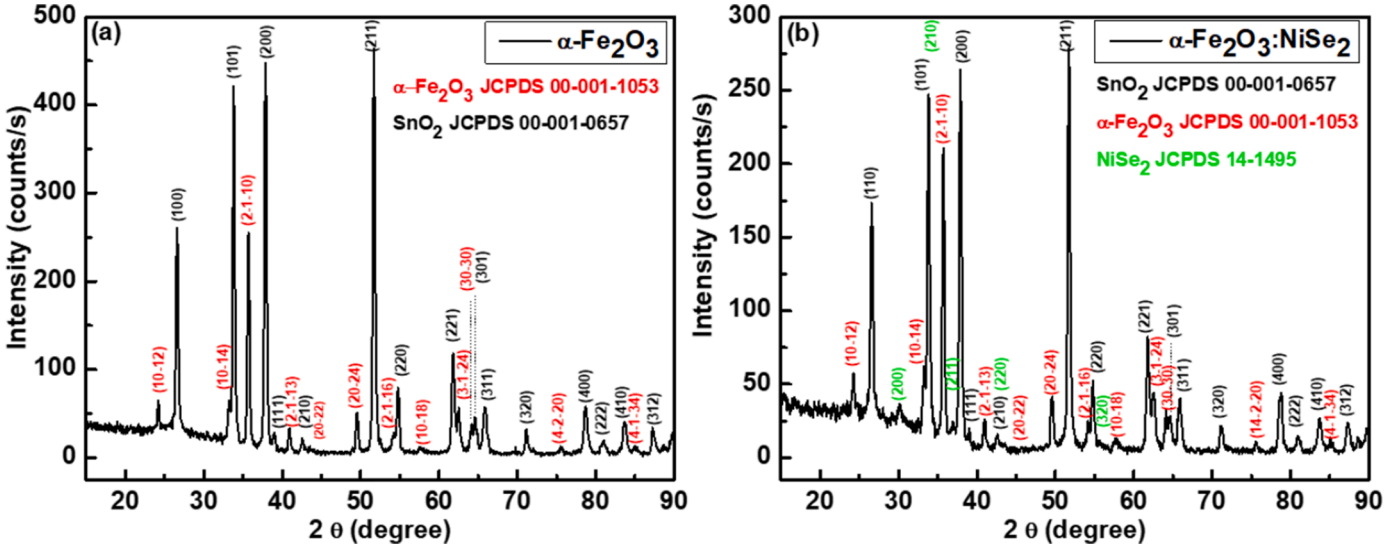

Fig. 4. XRD patterns for α-Fe_2O_3 (Red) and $NiSe_2$:α-Fe_2O_3 (Black) where facets are identified for SnO_2 (black), α-Fe_2O_3 (red), and $NiSe_2$ (green).

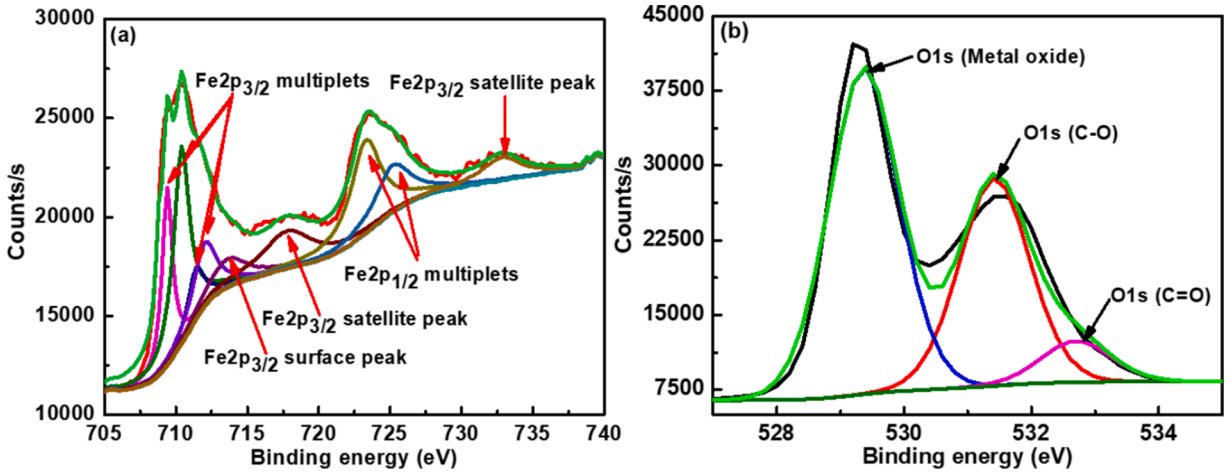

Fig. 5. High resolution XPS of α-Fe_2O_3 with depictions of (a) Fe 2p and (b) O 1 s scans.

Table 1
XPS data of α-Fe_2O_3 with depictions for Fe 2p and O 1 s scans.

α-Fe_2O_3 **Fe**	$Fe2p_{3/2}$ Multiplets				Surface	Satellite	$Fe2p_{1/2}$ Multiplets		Satellite
Peak/eV	709.4	710.4	711.4	712.0	713.6	717.8	723.3	725.2	732.8
FWHM/eV	0.43	0.67	0.71	0.98	1.65	2.22	1.27	1.50	1.70
α-Fe_2O_3 -> O									
	O1s (Metal Oxide)				O1s (C—O)			O1s (C = O)	
Peak/eV	529.6				531.2			532.8	
FWHM/eV	1.3				1.6			1.7	

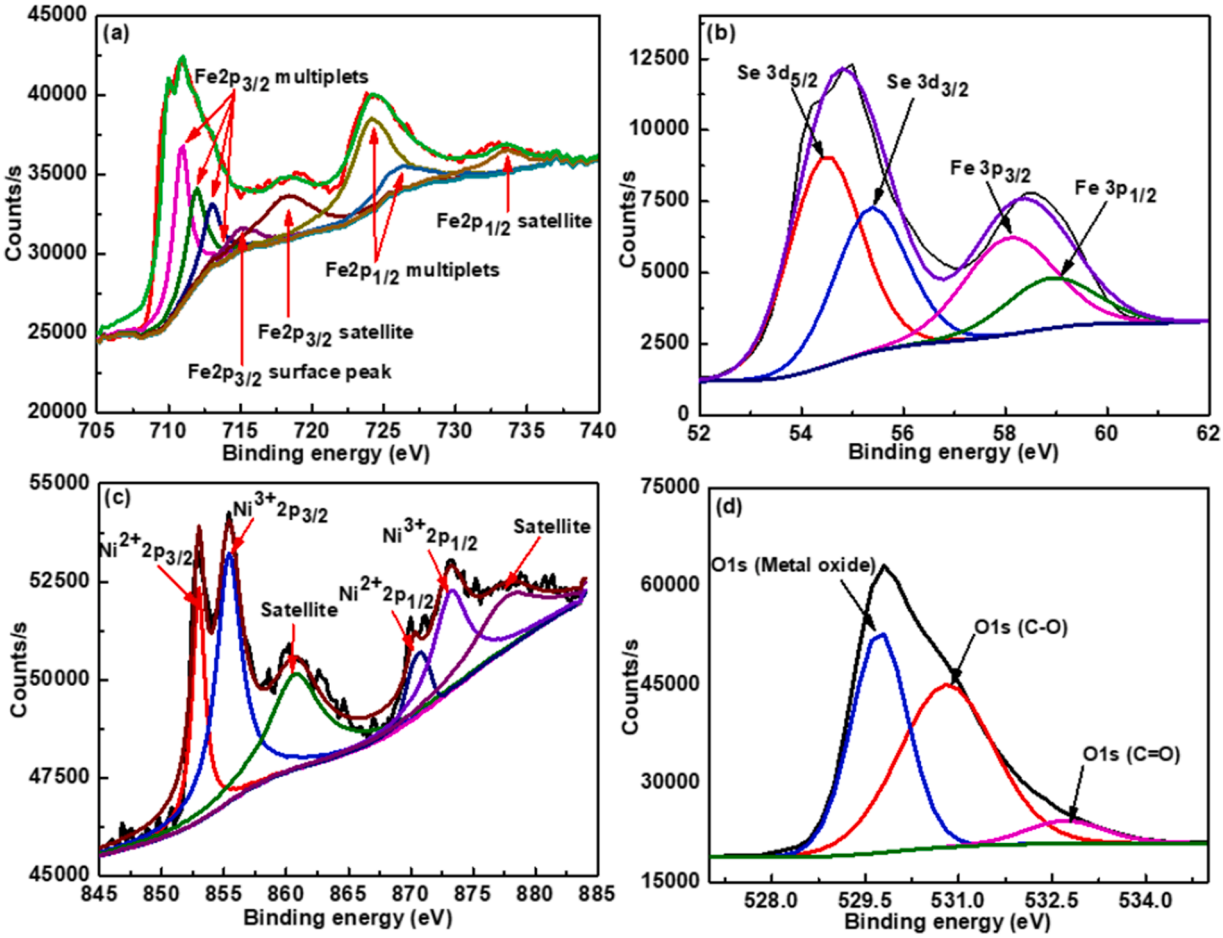

Fig. 6. High resolution XPS of α-Fe_2O_3:NiSe with depictions of (a) Fe, (b) Se, (c) Ni, and (d) O 1 s scans.

peak shapes were constrained to a Lorentzian/Gaussian of 30% mix ratio. Visual analyses of the sample surface as well as layer thickness were determined using a Zeiss Auriga field emission scanning electron microscope (SEM) operated at 5 kV. The cross-section SEM was used to determine active layer thickness in nm and these values were used in Hall Effect measurements conducted using an Ecopia HMS-3000 measuring system at 300 K, 500 μA and 0.55 T. This test provided the majority charge carrier concentration as well as charge mobility. The UV reflectance of the samples was performed using a Cary 5000 UV–Vis-NIR spectrophotometer equipped with an integrating sphere scanning from 200 to 2500 nm.

2.2.5. Photoelectrochemical characterization

The photoelectrochemical characterization was performed using an Autolab PGSTAT302N potentiostat. A three-electrode setup was implemented using a platinum wire counter electrode (Metrohm, Switzerland), 1 M KCl Ag/AgCl reference electrode (Metrohm, Switzerland), and the as-prepared materials as the working electrode. The cell containing an optical glass cube was covered with a solid covering to restrict ambient light interference. The cell contained a high-density polyethylene lid with sockets for electrodes and an opening on the side to allow in light from a solar simulator at 100 mW/cm^2. A 0.1 M NaOH electrolyte was used throughout. Electrochemical impedance spectroscopy (EIS) measurements were performed from 100,000 to 0.1 Hz using an AC voltage with an amplitude of 10 mV to determine charge transfer kinetics. EIS measurements were both performed in dark and solar simulated light conditions. The synthesis and testing procedures are depicted in Fig. 3.

Table 2
XPS data of α-Fe_2O_3:NiSe with depictions for Fe, Ni, Se, and O scans.

α-Fe_2O_3:NiSe -> Fe									
Fe	$Fe2p_{3/2}$ Multiplets				Surface	Satellite	$Fe2p_{1/2}$ Multiplets		Satellite
Peak/eV	710.9	711.9	713.0	714.0	715.0	718.2	724.1	726.0	733.6
FWHM/eV	0.43	0.67	0.71	0.98	1.65	2.22	1.27	1.50	1.70

α-Fe_2O_3:NiSe -> Ni						
	Ni^{2+} $2p_{3/2}$	Ni^{3+} $2p_{3/2}$	Ni $2p_{3/2}$ Satellite	Ni^{2+} $2p_{1/2}$	Ni^{3+} $2p_{1/2}$	Ni $2p_{1/2}$ Satellite
Peak/eV	852.9	855.4	860.7	870.3	873.2	877.7
FWHM/eV	0.6	1.2	2.5	0.6	1.7	3.1

α-Fe_2O_3:NiSe -> Se and Fe3p				
	$Se3d_{5/2}$	$Se3d_{3/2}$	Fe3p3/2	Fe3p1/2
Peak/eV	54.4	55.4	58.1	58.8
FWHM/eV	1.8	2.2	2.1	2.2

α-Fe_2O_3:NiSe -> O			
	O1s (Metal Oxide)	O1s (C—O)	O1s (C = O)
Peak/eV	529.7	530.8	532.7
FWHM/eV	1.1	1.8	1.5

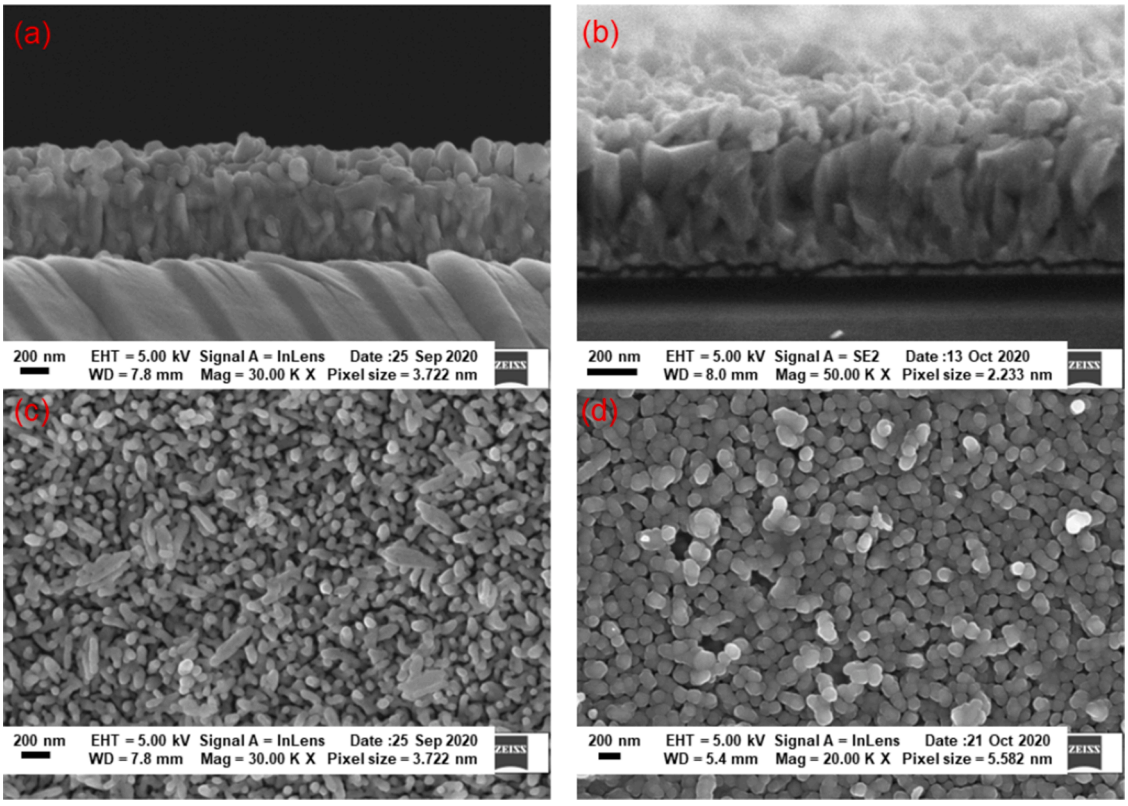

Fig. 7. SEM images of (a) Cross section of α-Fe_2O_3 (b) Cross section of α-Fe_2O_3:$NiSe_2$ (c) Top view of α-Fe_2O_3 and (d) Top view of α-Fe_2O_3:$NiSe_2$.

3. Results and discussion

3.1. Physical characterization

3.1.1. X-ray diffraction

The XRD patterns for both showed clear peaks for SnO_2 [24,25], and α-Fe_2O_3,[26,27] facets as seen in Fig. 4, providing evidence for the presence of these two materials. After electrodeposition, the $NiSe_2$:α-Fe_2O_3 XRD presented a new diffraction peak at 30.1 ° 2θ, a small peak at approximately 37 ° 2θ, a small peak between the (210) peak of SnO_2 and (20–22) peak of α-Fe_2O_3 and a peak could be seen on the shoulder of the (220) peak of SnO_2 at approximately 55.5 ° 2θ. The electrodeposition solution used would allow for the formation of Se (0), Ni (0), NiSe, Ni_2Se_3, and $NiSe_2$. The XRD patterns fit matches the $NiSe_2$ peaks [28–33], confirming the addition of $NiSe_2$. It is worth noting that the XRD patterns for SnO_2, α-Fe_2O_3, Se, Ni, NiSe, Ni_3Se_2, and $NiSe_2$ were adopted from previously calculated values by the Material Projects [24, 26,28–32].

3.1.2. X-ray photoelectron spectroscopy

XPS allowed for the surface characterization of the material and the results are presented in Fig. 5 (a-b), and Table 1. As shown in Fig. 5(a), the pristine α-Fe_2O_3 scan for Fe $2p_{3/2}$ and Fe $2p_{1/2}$ revealed the complex hematite XPS signature which authors have found to include a pre-peak,

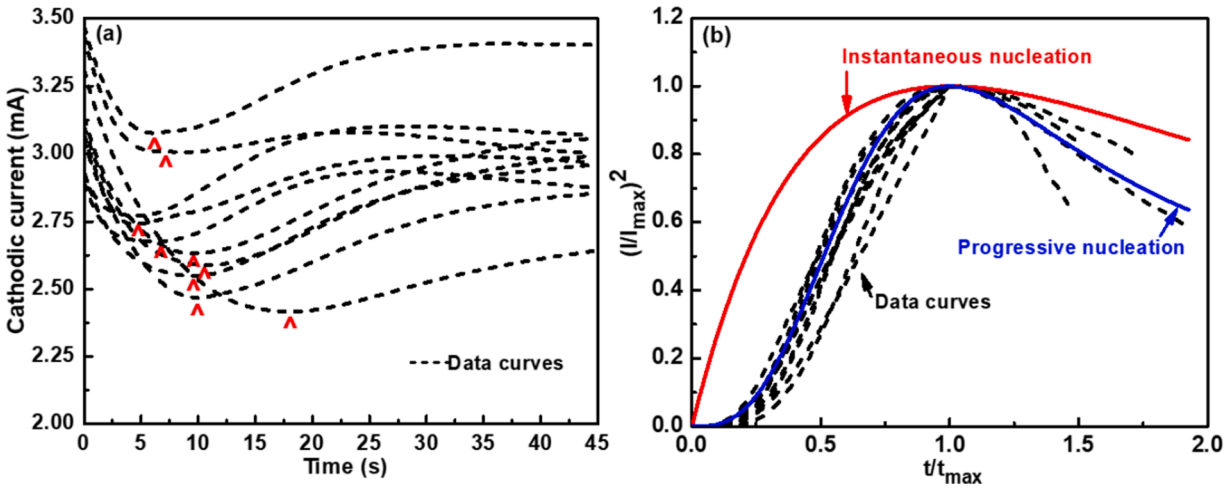

Fig. 8. (a) Current vs time for α-Fe_2O_3:$NiSe_2$ electrodeposition and (b) corresponding fit to nucleation models.

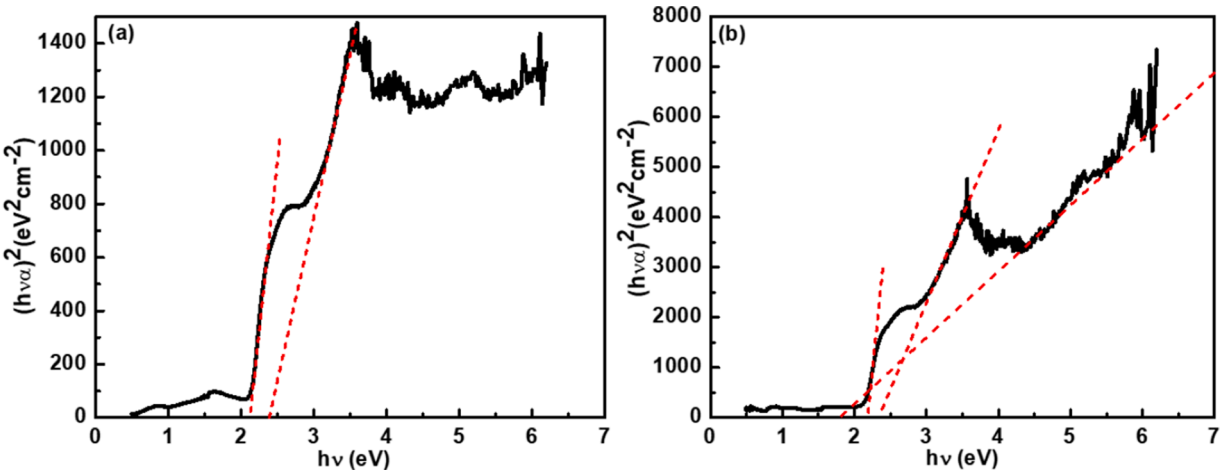

Fig. 9. Tauc plots for (a) α-Fe_2O_3 and (b) α-Fe_2O_3:$NiSe_2$.

4 multiplet splits of the Fe $2p_{3/2}$ peak, a Fe $2p_{3/2}$ surface peak, a Fe $2p_{3/2}$ satellite peak, 2 multiplet splits of the Fe $2p_{1/2}$, a surface Fe $2p_{1/2}$ peak, as well as a satellite Fe $2p_{1/2}$ peak, but not all of these, are always present [34–37]. The multiplet splitting is due to the effects of the core and valence open shell electrons angular momentum coupling, the ligand field splitting of the valence shell orbitals, and the degree of co-valent mixing of the O (2p) electrons with the Fe (3d) electrons [38]. In the pristine hematite sample, all these peaks were present with the notable exception of the Fe $2p_{1/2}$ surface peak, indicating a change to the surface of the sample which isn't seen in the consulted literature. The O 1 s spectra was fitted using three components corresponding to Fe-O binding energy within α-Fe_2O_3. The peak positions and full width half maximum (FWHM) are presented in Table 1.

The XPS surface characterization of the $NiSe_2$:α-Fe_2O_3 sample is presented in Fig. 6 (a-d) and Table 2. The Fe $2p_{3/2}$ and Fe $2p_{1/2}$ scans for the NiSe-treated hematite sample revealed some differences in the Iron surface content of the sample. Notably, the peaks are shifted to higher binding energies, ranging from a 0.4 eV shift in the Fe $2p_{3/2}$ satellite peak to 2.0 eV in the 4th Fe $2p_{3/2}$ multiplet. This may indicate that Iron at the surface of the $NiSe_2$:α-Fe_2O_3 sample has had its immediate chemical environment changed, and is often associated with an increase in oxidation state [39,40]. It seems unlikely that this would be the cause as the electrodeposition process should cathodically reduce the Iron oxide towards lower oxidation state products such as Fe_3O_4 or $Fe(OH)_2$, hence the change is more likely due to the presence of NiSe bonding onto the α-Fe_2O_3 and altering its local environment. Furthermore, the Fe $2p_{3/2}$ surface peak was reduced in size following electrodeposition but not entirely removed, suggesting to co-existence of $NiSe_2$ and Fe on the material surface. In addition, the Ni 2P spectra in Fig. 6(c) suggest the existence of Ni-Se and Ni-O bonds suggesting the electrodeposition of the $NiSe_2$ [41]. Furthermore, the existence $NiSe_2$ is supported by the XPS spectra of Se 2P in Fig. 6(b). The corresponding peak positions and full width half maximum (FWHM) suggesting the formation of the composite are presented in Table 2.

3.1.3. *Scanning electron microscopy*

SEM was employed to further characterize the surface morphology and overall thickness of the samples. The results are presented in Fig. 7 (a-d). The thickness of the active layer on the FTO was approximately 300 nm for the α-Fe_2O_3 sample Fig. 7(a) and approximately 218 nm for the α-Fe_2O_3:$NiSe_2$ sample Fig. 7(b). This decrease in layer thickness suggests that the α-Fe_2O_3 is reduced via cathodic reduction before or during the addition of $NiSe_2$. The surface of the samples, Fig. 7 (c-d), depict a rod-like morphology for α-Fe_2O_3 with and without α-$NiSe_2$, where the α-Fe_2O_3 sample has long, thin rods and the α-Fe_2O_3:$NiSe_2$ sample has shorter, wider rods. This evidence points to the deposition process involving the cathodic reduction of α-Fe_2O_3 rods followed by the deposition of $NiSe_2$ onto these stunted rods, widening them. The reason for the reaction changing midway is believed to be as a result of the initial reduction of α-Fe_2O_3 creating a high concentration of aqueous

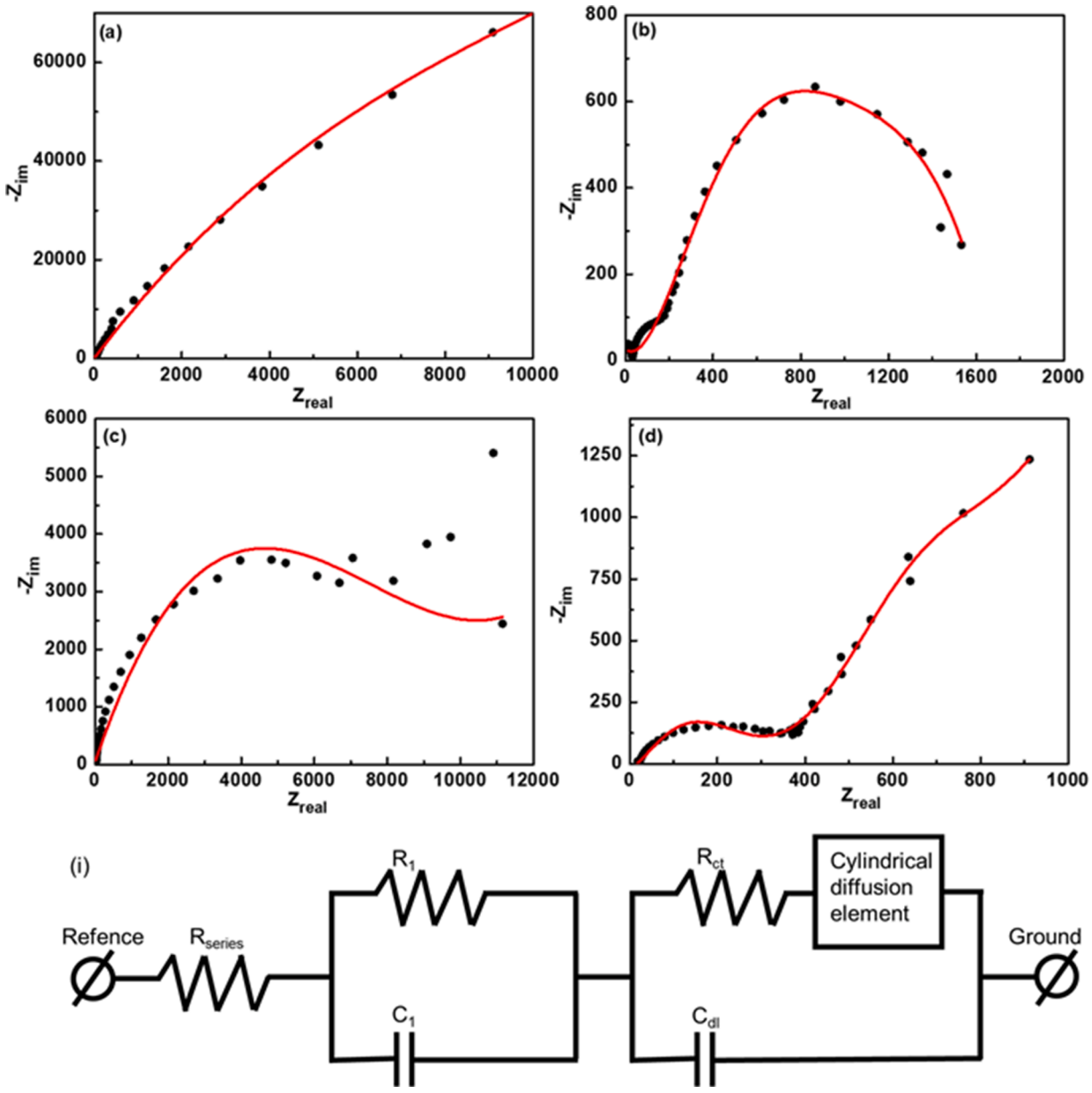

Fig. 10. Nyquist plots (a) in the dark and (b) in the light for α-Fe_2O_3, (c) in the dark and (d) in the light for α-Fe_2O_3:$NiSe_2$. (i) equivalent circuits in the dark for α-Fe_2O_3 and α-Fe_2O_3:$NiSe_2$.

Table 3
Fitted equivalent circuit parameters.

	α-Fe_2O_3 (dark)	α-Fe_2O_3 (light)	α-Fe_2O_3: $NiSe_2$ (dark)	α-Fe_2O_3: $NiSe_2$ (light)
Charge transfer resistance, R_{ct} (Ω)	172,607	1182	5346	208
Double layer capacitance, C_{dl} (F)	2.35×10^{-5}	2.19×10^{-4}	9.23×10^{-8}	1.85×10^{-4}

Iron species near the surface making the reduction reaction unfavorable.

3.1.4. Electrodeposition nucleation and growth regime analysis

To study the stepwise electrodeposition, the current-time transients for the electrodeposition process were examined. This procedure involved characterizing the growth of nuclei as instantaneous or progressive where the current is highest at $t = t_{max}$, and current $I = I_{max}$ [42]. In some electrodeposition experiments such as the one described in this work, the current measured begins at a high point before dropping to its minimum, $t = 0$, before progressing through its maximum. In these cases, the lowest point is re-labelled as $t = 0$ and $I = 0$ [43]. The instantaneous nucleation model depicts the formation of many nuclei initially and the further growth of new material occurring only on these nuclei. The progressive nucleation model depicts the constant formation of new nuclei as the material grows. The two models are graphed by the following equations:

$$\textit{Instantaneous nucleation}: \ (I/I_{max})^2 = \frac{1.9542}{t/t_{max}} \{1 - exp\ [-1.2564(t/t_{max})]\}^2 \quad (1)$$

$$\textit{Progressive nucleation}: \ (I/I_{max})^2 = \frac{1.2254}{t/t_{max}} \{1 - exp\ [-2.3367(t/t_{max}).^2]\}^2 \quad (2)$$

The current-time transients were collected during the 90 s deposition

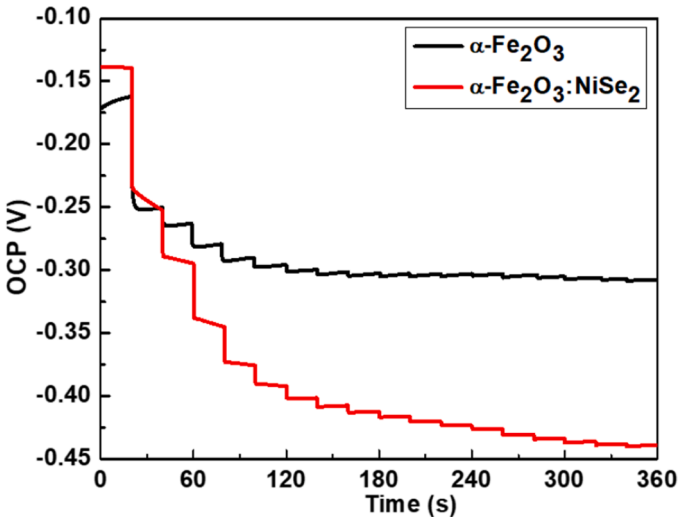

Fig. 11. OCP vs time for both samples.

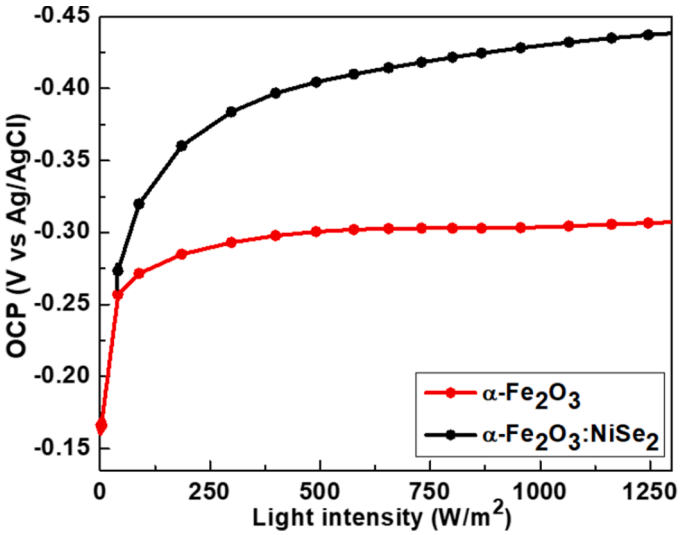

Fig. 12. Determination of OCP for α-Fe_2O_3 and Fe_2O_3:$NiSe_2$.

time for several samples. The minimum point for each curve was marked with a red pointer as seen in Fig. 8(a) which provided the $t = 0$ and $I = 0$ points for modeling seen in Fig. 8 (b). From this, it was clear that the nucleation and growth regime of $NiSe_2$ fitted the progressive model more closely than the instantaneous model. This coupled with the SEM results, provides convincing evidence that the electrodeposition occurs by initial stripping of the hematite followed by ongoing nucleation of $NiSe_2$ nanoparticles, resulting in the textured surface and reduced film thickness.

3.1.5. Hall effect measurements

The Hall Effect measurements allowed for the charge carriers concentration and mobility to be ascertained. The dominant charge carriers for both samples were electrons and the concentration of each was measured to be 2.009×10^{21} cm^{-3} for α-Fe_2O_3 and 9.574×10^{20} cm^{-3} for α-Fe_2O_3:$NiSe_2$, only 47.7% of the pristine hematite sample. This may be due to the introduction of electron holes provided by the $NiSe_2$. The mobility of the carriers was found to be 12.71 $cm^2V^{-1}s^{-1}$ for the α-Fe_2O_3 sample and 37.45 $cm^2V^{-1}s^{-1}$ for the α-Fe_2O_3:$NiSe_2$, an improvement of 294.6%. This is believed to be due to the greater conductivity [44] provided by $NiSe_2$.

3.1.6. UV/vis spectroscopy

For the optical characterization, UV/vis spectroscopy was used to determine the size of the band gap for both samples by measuring the reflectance over a wide range of light intensities. The reflectance values were converted to absorbance via the Kubelka-Munk function [45]. These absorbance values were then used to construct Tauc plots where the y-axis was set to $(h\nu\alpha)^2$. The Tauc plots presented in Fig. 9 (a-b) are very similar in shape up to a photon energy of 3.5 eV. In this region both samples produce two clear linear ranges which correspond to 2.1 eV and 2.3 eV for α-Fe_2O_3:$NiSe_2$, Fig. 9(a) and 2.1 eV and 2.4 eV for α-Fe_2O_3, Fig. 9(b). These results are close to the range of band gaps for α-Fe_2O_3 which have been reported to be between 1.9 and 2.2 eV,[46,14], and can be attributed to hematite. The reason for the existence of 2 linear ranges is attributed defects in hematite which narrow the bandgap,[47,48], and these defects may arise from the naturally occurring mixture of Fe^{2+} and Fe^{3+}present in hematite. Above 3.5 eV the Tauc plot for α-Fe_2O_3:$NiSe_2$ depicts an increase in the absorption which is not seen in the α-Fe_2O_3 sample. This roughly linear region produces a tentative band gap value of 1.8 eV, which is likely due to the addition of $NiSe_2$. Although there are few reports covering the optical characteristics of this material, one group has measured it to be approximately 1.65 Ev [49].

3.2. Photoelectronic characterization

3.2.1. Electrochemical impedance spectroscopy measurements

The findings from EIS measurements were interpreted by graphing Nyquist plots and were fitted using the software MEISP [50]. The α-Fe_2O_3 sample was fitted using an equivalent circuit comprised of an RC parallel in series with a diffusion element specifically modeled for cylinders [51] due to the cylindrical nature of the nanorods. As per the SEM images, the α-Fe_2O_3:$NiSe_2$ sample does not present with a cylindrical morphology and as such the equivalent circuit used was fitted via a general boundary unit diffusion parameter [52]. These circuits are presented with the fitted Nyquist plots in Fig. 10 (a-d). The α-Fe_2O_3:$NiSe_2$ sample had a greatly reduced (97% decrease) charge transfer resistance under no illumination and 82% decrease in the light as compared to the α-Fe_2O_3 sample. The full results of the circuit fittings are listed in Table 3.

3.2.2. Open circuit potential

The OCP and its change with light intensity were evaluated under illumination from a 7 W, 470 nm blue LED light source. The light intensity was steadily increased and allowed to stabilize after each incremental ramp which is depicted in Fig. 11. Each step change corresponded to an increase in light intensity. Every 20 s the light intensity was increased by increasing the driving voltage to the LED which caused a near-instant step change. The measurement was allowed to reach a steady state before taking the OCP value. For example, the first 20 s were in dark conditions and after the first exposure to light, the OCP reading was taken at 39 s, just before the next step increased.

The OCP measurements are shown in Fig. 12. From this, it is clear that the α-Fe_2O_3:$NiSe_2$ produced a stronger potential as compared to the α-Fe_2O_3 sample. This can be attributed to an increased carrier concentration or a higher current produced as a result of illumination [53]. As per Fig. 12, the electric field is seen to increase with OCP and so an increased OCP can produce a stronger electric field for charge separation and transport [23]. The α-Fe_2O_3 showed minuscule changes over a 500 W/m^2 light intensity. In contrast, the OCP for the α-Fe_2O_3:$NiSe_2$ sample continues to increase well beyond this point. This suggests that the MS junction effectively collects charge carriers as a result of the intrinsically larger diffusion lengths and charge carrier lifetimes.

3.2.3. Transient photocurrent

To further elucidate the charge transport, build-up, and recombination within the samples, transient photocurrent studies were performed on samples through intermittent illumination whilst measuring the

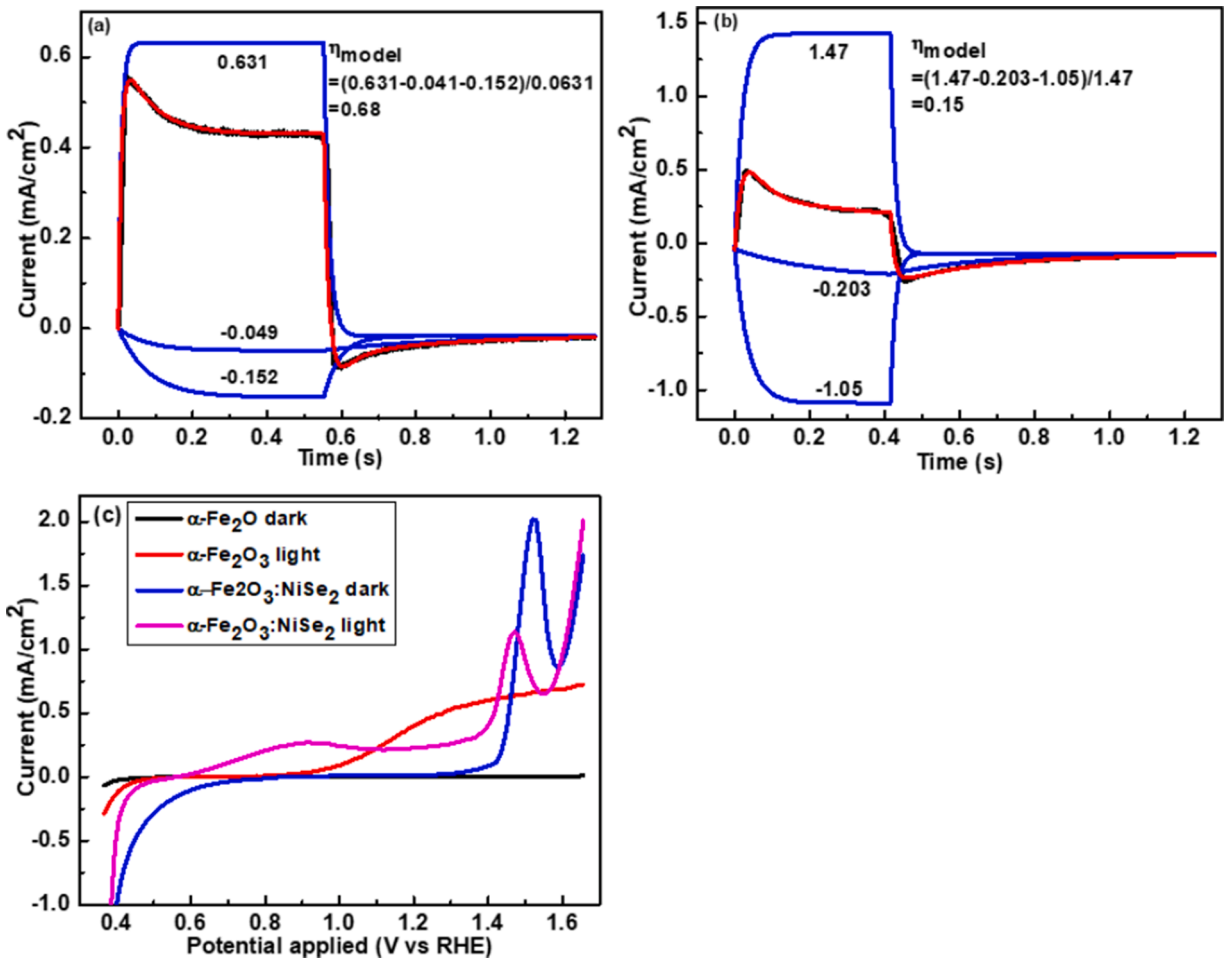

Fig. 13. Experimental results and fit to model for (a) α-Fe_2O_3 and (b) α-Fe_2O_3:$NiSe_2$. Black points are the experimental data, blue lines are the individual components of the fit and the red line is the overall fit produced by the sum of the components. (c) LSV of α-Fe_2O_3 and α-Fe_2O_3:$NiSe_2$.

output photocurrent. Each recorded photocurrent transient was fitted using a bi-phasic or tri-phasic exponential equation presented by Eq. (3):

$$I = A_1\left(1 - e^{-k_1 t}\right) + A_2\left(1 - e^{-k_2 t}\right) + A_3\left(1 - e^{-k_3 t}\right) \quad (3)$$

Where k is decay rate, t is time and A is fit coefficients. The positive terms (Eq. (3)) represent the bulk charge carrier generation and the negative terms depict the charge carrier recombination at the surface. Upon illumination, a sharp spike in current is observed as a result of surface reactions with the photogenerated charge carriers. This is followed by a decrease in current density which is ascribed to the diffusion of new reactants. Based on this a modeled efficiency, η_{model} was determined for each sample based on its fit coefficients (A-values). η_{model} describes the ratio of charge carriers removed and those produced in the bulk. This was done to evaluate the efficiency of charge transfer. A higher η_{model} value means a more efficient response to light resulting in higher photocurrent. The tri-phasic fit for the α-Fe_2O_3 and α-Fe_2O_3:$NiSe_2$ sample upon illumination was:

$$I = 0.631\left(1 - e^{-117t}\right) - 0.152\left(1 - e^{-12.5t}\right) - 0.049\left(1 - e^{-12.82t}\right) \quad (4)$$

$$I = 1.47\left(1 - e^{-49.2t}\right) - 1.05\left(1 - e^{-28t}\right) - 0.203\left(1 - e^{-4.39t}\right) \quad (5)$$

The experimental results as well as η_{model} calculation are presented in Fig. 13 (a-b). It can be seen from Fig. 13 that α-Fe_2O_3 produces higher photocurrent compared to α-Fe_2O_3:$NiSe_2$ thus having a higher η_{model}. This was further confirmed via LSV studies shown in Fig. 13(c). Interestingly, the α-Fe_2O_3 sample produced the weakest opec circuit potential (OCP) despite producing higher photocurrent compared to α-Fe_2O_3:$Nise_2$. This suggests that the α-Fe_2O_3:$NiSe_2$ sample stores the most charge carriers and generates the strongest electric field of the 2 samples but once the circuit is closed, these carriers are either not produced very fast or not transferred very fast, hindering photocurrent as described by the η_{model} efficiency and LSV data.

4. Conclusion

In this work, we report the synthesis of a α-Fe_2O_3:$NiSe_2$ thin film electrode via electrodeposition in the absence of a dehydration step or lattice parameter matching. The prepared samples optical and photoelectronic properties were greatly improved over their pristine α-Fe_2O_3 counterpart. The developed material demonstrated a highly reduced charge transfer resistance in light and dark conditions as well as producing a higher OCP and charge career mobility. Transient photocurrent measurements were employed to establish the efficiency of charge transfer and the relationship between charge transfer kinetics and film thickness was hypothesized based on the results. This method bares the potential to be highly scalable and offers the possibility of exploring many more combinations of α-Fe_2O_3 and metal selenide materials.

CRediT authorship contribution statement

Eran Visser: Writing – original draft. **Neville Cory:** Writing – review & editing. **Orlette Mkhari:** Writing – review & editing. **Jessica Chamier:** Data curation. **Franscious Cummings:** Data curation. **Mahabubur Chowdhury:** Conceptualization, Supervision, Writing –

review & editing.

Declaration of Competing Interest

The authors declare that they have no known competing financial interests or personal relationships that could have appeared to influence the work reported in this paper.

Data availability

Data will be made available on request.

Acknowledgements

The authors would like to thank the National Research Foundation for their contribution to this work (Reference number: MND190701452066) as well as the Cape Peninsula University of Technology.

References

[1] Q. Liu, et al., Morphology-controlled α-Fe2O3 nanostructures on FTO substrates for photoelectrochemical water oxidation, J. Alloys Compd. 715 (2017) 230–236, https://doi.org/10.1016/j.jallcom.2017.04.213.
[2] S. Shen, S.A. Lindley, X. Chen, J.Z. Zhang, Hematite heterostructures for photoelectrochemical water splitting: rational materials design and charge carrier dynamics, Energy Environ. Sci. 9 (9) (2016) 2744–2775, https://doi.org/10.1039/c6ee01845a.
[3] H.K. Dunn, et al., Tin doping speeds up hole transfer during light-driven water oxidation at hematite photoanodes, Phys. Chem. Chem. Phys. 16 (44) (2014) 24610–24620, https://doi.org/10.1039/c4cp03946g.
[4] K.Y. Yoon, et al., NiFeOx decorated Ge-hematite/perovskite for an efficient water splitting system, Nat. Commun. 12 (1) (2021) 1–12, https://doi.org/10.1038/s41467-021-24428-7.
[5] J.Y. Kim, et al., Single-crystalline, wormlike hematite photoanodes for efficient solar water splitting, Sci. Rep. (2013) 1–8, https://doi.org/10.1038/srep02681.
[6] J. Su, J. Wang, C. Liu, B. Feng, Y. Chen, L. Guo, On the role of metal atom doping in hematite for improved photoelectrochemical properties: a comparison study, RSC Adv. 6 (104) (2016) 101745–101751, https://doi.org/10.1039/c6ra22895j.
[7] H. Ahn, K. Yoon, M. Kwak, J. Park, J. Jang, Boron-doping of metal-doped hematite for reduced surface recombination in water splitting, ACS Catal. (2018), https://doi.org/10.1021/acscatal.8b03184.
[8] F. Li, et al., Construction of an efficient hole migration pathway on hematite for efficient photoelectrochemical water oxidation, J. Mater. Chem. A Mater. 6 (46) (2018) 23478–23485, https://doi.org/10.1039/C8TA07832G.
[9] D.K. Bora, et al., Functionalization of nanostructured hematite thin-film electrodes with the light-harvesting membrane protein C-phycocyanin yields an enhanced photocurrent, Adv. Funct. Mater. 22 (3) (2012) 490–502, https://doi.org/10.1002/adfm.201101830.
[10] S. Chen, et al., Metal selenides for photocatalytic Z-scheme pure water splitting mediated by reduced graphene oxide, Chin. J. Catal. 40 (Nov. 2019) 1668–1672, https://doi.org/10.1016/S1872-2067(19)63326-7.
[11] R. Schneider, L. Bal, Hydrothermal routes for the synthesis of CdSe core quantum dots. State-of-the-Art of Quantum Dot System Fabrications, 2012, https://doi.org/10.5772/34977.
[12] F.A. Rasmussen and K.S. Thygesen, "Computational 2D materials database : electronic structure of transition-metal dichalcogenides and oxides," 2015, doi: 10.1021/acs.jpcc.5b02950.
[13] H.L. Zhuang and R.G. Hennig, "Computational search for single-layer transition-metal dichalcogenide photocatalysts," 2013, doi: 10.1021/jp405808a.
[14] Y. Xu, M.A.A. Schoonen, The absolute energy positions of conductionand valence bands of selected semiconducting materials, Am. Mineral. 85 (2000) 543–556.
[15] R.S. Selinsky, S. Shin, M.A. Lukowski, S. Jin, Epitaxial heterostructures of lead selenide quantum dots on hematite nanowires, J. Phys. Chem. Lett. 3 (2012) 1649–1656, https://doi.org/10.1021/jz300672x.
[16] J. Barthel, R. Deiss, The limits of the Pourbaix diagram in the interpretation of the kinetics of corrosion and cathodic protection of underground pipelines, Mater. Corros. 72 (3) (2021) 434–445, https://doi.org/10.1002/maco.202011977.
[17] Y. Kim, J. Kim, Corrosion behavior of pipeline carbon steel under different iron oxide deposits in the district heating system, Metals (Basel) 7 (182) (2017), https://doi.org/10.3390/met7050182.
[18] K. Xie, A.R. Kamali, Electro-reduction of hematite using water as the redox mediator, Green Chem. 21 (198) (2019), https://doi.org/10.1039/c8gc02756k.
[19] J. Yu, Y. Han, Y. Li, P. Gao, W. Li, Mechanism and kinetics of the reduction of hematite to magnetite with CO – CO_2 in a micro-fluidized bed, Minerals 7 (209) (2017), https://doi.org/10.3390/min7110209.
[20] D.V. Lopes, Y.A. Ivanova, A.V. Kovalevsky, A.R. S.arabando, J.R. F.rade, M.J. Q. uina, Electrochemical reduction of hematite-based ceramics in alkaline medium : challenges in electrode design, Electrochim. Acta 327 (2019), https://doi.org/10.1016/j.electacta.2019.135060.
[21] B. Pandit, D.P. D.ubal, P. Gómez-Romero, B.B. K.ale, B.R. S.ankapal, V_2O_5 encapsulated MWCNTs in 2D surface architecture: complete solid-state bendable highly stabilized energy efficient supercapacitor device, Sci. Rep. 7 (2017) 1–12, https://doi.org/10.1038/srep43430.
[22] D.B. X.ochitl, S. Sevda, K. Vanbroekhoven, D. Pant, The accurate use of impedance analysis for the study of microbial electrochemical systems, Chem. Soc. Rev. 41 (21) (2012) 7228–7246, https://doi.org/10.1039/c2cs35026b.
[23] K.-.H. Ye, et al., Enhancing photoelectrochemical water splitting by combining work function tuning and heterojunction engineering, Nat. Commun. 10 (1) (2019) 3687, https://doi.org/10.1038/s41467-019-11586-y.
[24] The Materials Project. *Materials Data on SnO_2 by Materials Project*, United, States: N, 2020, https://doi.org/10.17188/1272823.
[25] R. Kupila, K. Lappalainen, T. Hu, A. Heponiemi, D. Bergna, U. Lassi, Production of ethyl lactate by activated carbon-supported Sn and Zn oxide catalysts utilizing lignocellulosic side streams, Appl. Catal. A Gen. 624 (2021), 118327, https://doi.org/10.1016/j.apcata.2021.118327.
[26] The Materials Project. *Materials Data on Fe_2O_3 by Materials Project*, United, States: N, 2020, https://doi.org/10.17188/1677177.
[27] M. Hjiri, N.H. Alonizan, M.M. A.lthubayti, S. Alshammari, H. Besbes, M.S. A.ida, Preparation and photoluminescence of $NiFe_2O_4$ nanoparticles, J. Mater. Sci 30 (16) (2019) 15379–15387, https://doi.org/10.1007/s10854-019-01914-9.
[28] The Materials Project. *Materials Data on Se by Materials Project*, United, States: N, 2020, https://doi.org/10.17188/1189869.
[29] The Materials Project. *Materials Data on Ni by Materials Project*, United, States: N, 2020, https://doi.org/10.17188/1199153.
[30] The Materials Project. *Materials Data on NiSe by Materials Project*, United, States: N, 2020, https://doi.org/10.17188/1281394.
[31] The Materials Project. *Materials Data on Ni_3Se_2 by Materials Project*, United, States: N, 2020, https://doi.org/10.17188/1195708.
[32] The Materials Project. *Materials Data on $NiSe_2$ by Materials Project*, United, States: N, 2020, https://doi.org/10.17188/1196097.
[33] Z. Yue, G. Wu, X. Chen, Y. Han, L. Liu, Q. Zhou, Facile, room-temperature synthesis of NiSe2 nanoparticles and its improved performance with graphene in dye-sensitized solar cells, Mater. Lett. 192 (2017) 84–87, https://doi.org/10.1016/j.matlet.2016.12.053.
[34] A.P. Grosvenor, B.A. K.obe, M.C. Biesinger, and N.S. Mcintyre, "Investigation of multiplet splitting of Fe 2p XPS spectra and bonding in iron compounds," no. October, pp. 1564–1574, 2004, doi: 10.1002/sia.1984.
[35] G.F. Moreira, E.R. Peçanhab, M.B.M. Monte, L.S.L. Filho, F. Stavale, XPS study on the mechanism of starch-hematite surface chemical complexation, Miner. Eng. 110 (2017) 96–103, https://doi.org/10.1016/j.mineng.2017.04.014. April.
[36] M. Wang, H. Hu, Q. Chen, and G. Ji, "FT-IR, XPS, and DFT Study of Adsorption Mechanism of Sodium Acetohydroxamate onto Goethite or Hematite," vol. 29, no. 3, pp. 308–318, 2016, doi: 10.1063/1674-0068/29/cjcp1508182.
[37] S. Bai, Z. Ding, X. Fu, C. Li, C. Lv, and S. Wen, "Investigations on soluble starch as the depressant of hematite during flotation separation of apatite," vol. 55, no. 1, pp. 38–48, 2019, doi: 10.5277/ppmp18108.
[38] P.S. Bagus, C.J. Nelin, C.R. Brundle, N. Lahiri, E.S. Ilton, K.M. Rosso, Analysis of the Fe 2p XPS for hematite α Fe $_2$ O $_3$: consequences of covalent bonding and orbital splittings on multiplet splittings, J. Chem. Phys. 152 (1) (Jan. 2020), 014704, https://doi.org/10.1063/1.5135595.
[39] C. Dallera, L. Braicovich, L. Duò, A. Palenzona, G. Panaccione, G. Paolicelli, B.C. C. Cowie, J. Zegenhagen, Hard X-ray photoelectron spectroscopy: sensitivity to depth, chemistry and orbital character, Nucl. Instrum. Methods Phys. Res. A 547 (2005) 113–123, https://doi.org/10.1016/j.nima.2005.05.017.
[40] T.C. T.aucher, I. Hehn, O.T. H.ofmann, M. Zharnikov, and E. Zojer, "Understanding chemical versus electrostatic shifts in x ray photoelectron spectra of organic self-assembled monolayers," 2016, doi: 10.1021/acs.jpcc.5b12387.
[41] Y. Zhang, S.Y. Yuan, Y. Zou, T.T. Li, H. Liu, J.J. Wang, Enhanced charge separation and conductivity of hematite enabled by versatile NiSe2 nanoparticles for improved photoelectrochemical water oxidation, Appl. Mater. Today 28 (Aug. 2022), https://doi.org/10.1016/j.apmt.2022.101552.
[42] B. Scharifker, G. Hills, Theoretical and experimental studies of multiple nucleation, Electrochim. Acta 28 (2) (1982) 879–889.
[43] S. Bijani, R. Schrebler, E.A. Dalchiele, M. Gabás, L. Martínez, J.R. Ramos-Barrado, Study of the nucleation and growth mechanisms in the electrodeposition of micro- and nanostructured Cu_2O thin films, J. Phys. Chem. C 115 (43) (2011) 21373–21382, https://doi.org/10.1021/jp208535e.
[44] K.I. Bolotin, 9 - Electronic transport in graphene: towards high mobility, in: V. Skákalová, A.B. Kaiser (Eds.), Graphene, Woodhead Publishing, 2014, pp. 199–227, https://doi.org/10.1533/9780857099334.3.199.
[45] P. Kubelka, F. Munk, An article on optics of paint layers, Tech. Phys. 12 (1931) 593–601.
[46] J. Guo, Electronic structure characterization and bandgap engineering of solar hydrogen materials, Sol. Hydrogen Nanotechnol. II (2007), https://doi.org/10.1117/12.734618.
[47] S.K. Padhi and M.G. Krishna, Non-Classical Crystal Growth Recipe using nanocrystalline ceria a detailed review, *arXiv preprint*, no. November 2019.
[48] P. Yang, J. Chu, Modified structural, optical, magnetic and ferroelectric properties in (1-x) BaTiO3-xBaCo0.5Nb0.5O3-δ ceramics, Ceram. Int. (2019) 1–6, https://doi.org/10.1016/j.ceramint.2019.11.068. November.
[49] T.J.S. Anand, M. Zaidan, S. Shariza, Effect of additives on optical measurements of NiSe2 thin films, Procedia. Eng. 53 (2013) 555–561, https://doi.org/10.1016/j.proeng.2013.02.071.

[50] D. Harrington, Multiple electrochemical impedance spectra parameterization (MEISP+), J. Am. Chem. Soc. 124 (7) (2002) 1554–1555.
[51] T. Jacobsen, K. West, Diffusion impedance in planar, cylindrical and spherical symmetry, Electrochim. Acta 40 (2) (1995) 255–262, https://doi.org/10.1016/0013-4686(94)E0192-3.
[52] D.R. Franceschetti, J.R. Macdonald, Interpretation of finite-length-warburg-type impedances in supported and unsupported electrochemical cells with kinetically reversible electrodes, J. Electrochem. Soc. 138 (5) (1991) 1368–1370, https://doi.org/10.1149/1.2085788.
[53] R.A. Sinton, A. Cuevas, Contactless determination of current-voltage characteristics and minority-carrier lifetimes in semiconductors from quasi-steady-state photoconductance data, Appl. Phys. Lett. 69 (17) (Oct. 1996) 2510–2512, https://doi.org/10.1063/1.117723.